Co-Mo-B Nanoparticles as a non-precious and Efficient Bifunctional Electrocatalyst for Hydrogen and Oxygen Evolution

S.Gupta[a*], N.Patel[a*], R.Fernandes[a], S.Hanchate[a], A.Miotello[b] and D. C. Kothari[a]

[a]Department of Physics and National Centre for Nanosciences & Nanotechnology, University of Mumbai, Vidyanagari, Santacruz (E), Mumbai 400098, India.

[b]Dipartimento di Fisica, Università degli Studi di Trento, I-38123 Povo (Trento), Italy

* Corresponding Author: **Suraj Gupta, Nainesh Patel**

Address: University of Mumbai,
Department of Physics,
Vidyanagari, Santacruz (E),
Mumbai 400 098, India
Tel. No.: +91-7208368335
Fax No.: +91-22-26529780
E-mail address:gsuraj.physics@gmail.com
nainesh11@gmail.com

Abstract:

The development of low-cost and non-toxic bifunctional electrocatalysts that can catalyse both hydrogen and oxygen evolution reactions (HER and OER) is of prime importance to accelerate the upscale of water electrolysis technology. Herein, we report for the first time, Co-Mo-B as one such bifunctional catalyst, prepared by a facile reduction method. The optimized catalyst, Co-3Mo-B showed excellent HER performance and achieves a current

density of 10 mA/cm^2 at mere 96 and 66 mV (vs RHE) in pH 7 and pH 14, respectively. High stability (40 hours) and reusability (5000 cycles) were obtained in both media. Co-3Mo-B nanoparticles were found to be made up of nano-sized crystalline domains, separated by grain boundaries containing active under-co-ordinated sites.The improved activity of Co-Mo-B could also be attributed to the formation of well dispersed nanoparticles of Co-Mo-B with increased specific and electrochemical surface area, as observed from morphological, physico-chemical and electrochemical analyses. Under alkaline conditions, Co-3Mo-B exhibited bifunctional characteristic as it could also produce oxygen at meagre overpotentials (320 mV to achieve 10 mA/cm^2) with favourable stability. Bifunctional property was also confirmed by employing Co-3Mo-B in a 2-electrode alkaline cell to execute overall water splitting to produce 10 mA/cm^2 at just 1.69 V, which was maintained for at least 25 hours of operation. The nature of the catalyst to form Co oxide/hydroxide species on the surface is responsible for good OER performance. The excellent activity of Co-3Mo-B makes it the best metal boride bifunctional electrocatalyst and future research in this area can diminish the gap to replicate the performance of noble metal catalysts such as Pt and RuO_2.

Introduction:

The idea of H_2-driven economy demands rapid development of key H_2 production techniques such as electrochemical and photo-electrochemical water splitting. Electrochemical water splitting, through renewable energy sources, is considered as one of the cleanest and simplest techniques to produce fuel-cell grade H_2. However, cost and natural abundance of electrode materials, play a decisive role in its large-scale

implementation. A general strategy involves replacing the noble group elements (Pt, Pd, Ru, etc.) by transition metal based catalysts. Over the past years, the viability of transition metal phosphides [1-3], sulphides [4-5], selenides [6-7], carbides [8-9] and nitrides [10-11] for hydrogen evolution reaction(HER) is very well established. In spite of these advances, none of these non-precious catalysts have been able to compete with noble group elements on site-specific activities [12]. Also, most of these catalysts face stability issues in alkaline media [12], whereas the present industrial electrolyzers operate in alkaline conditions. Another major concern is that industrial electrolyzers operate at voltages of 1.8 – 2 V, a whopping 40-50 % more voltage than the ideal case (1.23 V). A large fraction of this energy is spent to overcome the barrier of oxygen evolution reaction (OER). Even after a decade long research on OER materials, the quest for a catalyst that can reduce the overpotential considerably, is still in pursuit. In the wake of present issues, it is highly desirable to obtain a single catalyst, made up of transition metals, to catalyse HER and OER equally well. There have been a number of reports on non-precious metal catalysts that show bifunctional characteristic in alkaline media, such as Ni-P/NF [13], FeP nanotubes [14], Co-Se/Ti [15], Co-P MNA [16], $Fe_{10}Co_{40}Ni_{40}P$ [17] and so on. Recently, a renewed interest has surged in using transition metal borides (TMBs) for electrocatalytic applications [9, 18, 19, 20]. Mono-metal borides such as Co-B [18], Ni-B [19], Mo-B [9] have shown significant promise for HER in different pH conditions. Also, Co_2B annealed at 500 °C (Co_2B-500) [21] was recently presented as a bifunctional catalyst active in alkaline media. The superior performance of amorphous TMBs is due to the reverse electron transfer from boron to metal, providing higher electron density at these catalytic sites [18-20].From recent literature, one could see that ternary Co-based catalysts such as CoMoP [22], CoFeP [23], CoMoS [24], $CoMoS_2$ [25], CoNiB [20], which contain an additional transition metal, show improved electrochemical response

compared to their mono-metallic counterparts, owing to the synergy created between the two metals.

In the light of these ideas, we report Co-Mo-B nanoparticles (NPs), made up of low-cost, non-toxic elements, as an efficient catalyst for HER in neutral and alkaline media. From the morphological, physico-chemical and electrochemical analysis, it is shown that the addition of a small amount of Mo leads to a significant improvement in HER activity due to the formation of well dispersed NPs with increased specific and electrochemical surface area. Co-Mo-B is also found to be equally active and stable for OER in alkaline media. The present results for Co-Mo-B catalyst supersede the reported results of Co_2B-500 [21] and as on date, Co-Mo-B stands out to be the best TMB bifunctional electrocatalyst available.

Experimental Details:

Synthesis of catalysts. Co-Mo-B catalyst was synthesized by reducing the aqueous mixture of cobalt chloride and sodium molybdate in presence of $NaBH_4$. The molar ratio of metal (Co + Mo) to $NaBH_4$ was taken as 1:3 to ensure complete reduction of Co and Mo ions. On addition of $NaBH_4$, in a fraction of seconds, the aqueous solution turns black with lots of effervescence. Once the effervescence ceases, the solution was centrifuged to separate the remnant black powder which was later cleaned with double distilled water (DDW) and ethanol to remove unreacted ions and other impurities. The cleaned powder was then vacuum dried at room temperature to obtain the final nanocatalyst. The proportion of Mo in Co-Mo-B was varied by adjusting the molar ratio of Mo/(Mo+Co) in the starting aqueous mixture (from 1% to 9%). For comparative studies, Co-B powder was also synthesized without using Mo salt in the initial solution.

Material Characterization. Structural characterization of Co-Mo-B catalyst was performed by conventional X-Ray Diffractometer (RigakuUltima IV) using the Cu K_α radiation (λ = 1.5414 Å) in Bragg-Brentano (θ-2θ) configuration. The surface morphology of the catalyst samples was analyzed by a scanning electron microscope (SEM-FEG, INSPECT F50, FEI). A transmission electron microscope (TEM) (FEI Tecnai G2, F30 TEM microscope operating at an accelerating voltage of 300 kV) was used to obtain the particle size distribution. HR–TEM image and selected area electron diffraction (SAED) pattern were also recorded. EDX elemental mapping was performed in scanning TEM mode. X-ray photoelectron spectroscopy (XPS) was used to determine the surface electronic states and the related atomic composition of the catalysts. XPS was acquired using a monochromatic Al K_α (1486.6 eV) X-ray source and a hemispherical analyzer using a PHI 5000 Versa Probe II instrument. The BET surface area and adsorption-desorption isotherms were determined by nitrogen adsorption at 77 K (Micromeritics ASAP 2010) after degassing the powders at a temperature of 423 K for 2 hrs.

Preparation of catalyst modified glassy carbon (GC) electrode. A 3 mm glassy carbon electrode was polished to remove all sorts of contaminants from the surface. 5 mg of the desired catalyst was dispersed in 1 ml ethanol, with 10 µL of 5% Nafion, under continuous sonication, to obtain a homogenous catalyst ink. 30 µL of this ink (in steps of 10 µL) was drop-casted onto the GC surface and dried under IR lamp irradiation to obtain a uniform catalyst film with geometric surface area of 0.07 cm^2 and a mass loading of ~2.1 mg/cm^2.

Electrochemical measurements. All the electrochemical measurements were performed using a potentiostat-galvanostat system (PGSTAT 30) from Autolab equipped with facility to carry out electrochemical impedance spectroscopy (EIS). The electrochemical cell was a

borosilicate beaker, using a conventional three electrode design with catalyst modified GC electrode as the working electrode, a saturated calomel electrode as the reference and a Pt sheet (0.5 cm^2) as the counter electrode. Previously reported method [26] was used to calibrate the reference electrode with respect to reversible hydrogen electrode (RHE). For calibration, the calomel electrode was immersed in a H_2 saturated H_2SO_4 solution where one Pt sheet served as the counter while another Pt sheet as the working electrode. CV scans at a rate of 1 mV/s were recorded and average of the two potentials, where current becomes zero, was considered as the thermodynamic potential for HER. The measured potentials were later converted to RHE by adding a value of 0.241 + (0.05916 x pH). In 0.5 M KPi, E(RHE) = E(SCE) + 0.655 and in 1 M NaOH, E(RHE) = E(SCE) + 1.068.

The actual polarization measurements for HER and OER were performed at a sweep rate of 5 mV/s under continuous stirring (~ 900 rpm) to avoid bubble accumulation over the GC electrode. The series resistance (R_s) values were determined using impedance measurement data to compensate for iR losses (R_s = 3 Ω and 1 Ω for pH = 7 and 14 respectively). Tafel slope and exchange current density values were obtained by linear fitting the plot of log (i) versus overpotential (η) in the range of η = 0 - 250 mV. Turnover frequency (TOF) value was determined using the method reported in our previous work [20]. BET technique was used to establish the actual surface area of the Co-3Mo-B catalyst used for the TOF calculations. Long-term stability in potentiostatic mode was examined by maintaining the potential at a constant value and measuring the resultant current density for long hours. Recycling behavior of the catalyst for HER was tested by conducting cyclic voltammetric sweep for 5000 cycles with a scan rate of 100 mV/s.

Determination of Electrochemical Surface Area (ESA). The electrochemical capacitance was determined by sweeping the potential in the window of 100 mV on either sides of open-circuit potential (OCP) in 0.1 M Na_2SO_4 solution [19], at increasing scan rates of 20, 40, 60, 80 and 100 mV/s. Usually, in the potential range of 100 to 150 mV from OCP, no Faradaic processes are involved and the current obtained is due to charging and discharging of the capacitive double layer (C_{dl}). The difference in the capacitive currents ($\Delta j = |j_{cathodic} - j_{anodic}|$) were measured at -0.2 V for bare GC, -0.4 V for Co-B and -0.15 V for Co-3Mo-B catalysts, corresponding to all scan rates. This difference in capacitive current was then plotted against the respective scan rates, as shown in Fig. 3f. The slope of this graph gives the value of specific capacitance, which is an indicator of the electrochemical surface area of the catalyst.

Results and Discussion:

Co-Mo-B NPs were synthesized by reducing the aqueous mixture of cobalt and molybdenum salts with sodium borohydride. A series of samples were prepared with different molar concentrations of Mo with respect to Co [Mo/(Mo+Co)]. These samples are hereby denoted as Co-xMo-B, where x indicates the molar ratio [Mo/(Mo+Co)] (x = 1, 3, 5, 7, 9). Co-B NPs were also synthesized for comparative study. The electrochemical performance of the prepared catalysts was evaluated for HER by loading them on a polished glassy carbon (GC) electrode. The catalyst modified GC electrode was then tested in neutral and alkaline media, in a 3 electrode system equipped with a saturated calomel electrode as reference and a Pt electrode as counter. Fig. S1 shows the polarization curves for Co-Mo-B catalyst with different Mo/(Mo+Co) ratios varying from 1% to 9%, measured in pH 7 phosphate buffer. HER activity improved with the increase in Mo content up to Mo/(Mo+Co) = 3% and then

decreased again. Co-3Mo-B catalyst, with best HER activity, was chosen for further measurements. Co-3Mo-B catalyst was first tested in neutral medium to establish its effectiveness for HER under benign pH conditions. Fig.1a shows the linear sweep curves recorded for Co-3Mo-B catalyst along with Co-B and Pt electrode for comparison. All the curves were iR corrected by measuring their R_{ohmic} values using EIS, and the current densities were normalized to the geometric surface area of the bare GC electrode. Co-3Mo-B shows a negligible onset potential and could achieve the benchmark current density of 10 mA/cm^2 at mere 96 mV (vs RHE) which is just 46 mV higher than that obtained with Pt sheet electrode. When the cathodic potential is increased further, the current density rises sharply and higher current densities of 20 mA/cm^2 and 40 mA/cm^2 were reached at 141 mV and 213 mV, respectively, for Co-3Mo-B catalyst. The overpotential values reported here forCo-3Mo-B catalyst are significantly lower than those reported for Co-B (197 mV for 10 mA/cm^2) and all other metal boride catalysts, active in pH 7, with the exception of NiB_x films [19] which show even lower overpotential (~54 mV) also owing to its nanostructured film assembly. Co-3Mo-B outclasses many other non-noble HER catalysts, such as CoN_x/C [10], Mo_2C@NC [8], Cu(0) catalyst [27],WP NAs/CC [28],Fe-P/CC[29] andH_2-Cocat[30], employed in pH 7 (TableS1). Tafel plot analysis (Fig.1c) yields Tafel slope values of 56 mV/dec, 71 mV/dec and 38 mV/dec for Co-3Mo-B, Co-B and Pt electrode. The lower value of Tafel slope again indicates better HER kinetics. A Tafel slope value of 56 mV/dec for Co-3Mo-B suggests the dominance of Volmer-Heyrovsky reaction mechanism. By extrapolation of the graph used for Tafel slope analysis, exchange current densities were determined for Co-3Mo-B (1.20 mA/cm^2) which is much higher than that of Co-B and that of many other non-noble HER catalysts in pH 7 (Table S1).

As Co-B is known to work well in alkaline media [20, 21], the HER performance of Co-3Mo-B catalyst was also tested in 1 M NaOH (pH 14). Fig.1b shows linear sweep curves for Co-3Mo-B, Co-B and Pt electrode in pH 14 recorded at a scan rate of 5mV/s. Co-3Mo-B produces exceedingly high current densities at very meagre overpotentials. The current densities of 10, 50 and 100 mA/cm^2 were achieved at 66 mV, 145 mV and 184 mV, respectively for Co-3Mo-B while that for Pt required 36, 81 and 92 mV, respectively. The overpotentials for Co-3Mo-B catalyst are amongst the lowest values reported for any non-noble HER electrocatalyst, lower than that of NiB_x films [19], CoN_x/C [10], NiO/Ni-CNT [31], Mo_2C/NCNT [32], $Ni_{0.33}Co_{0.67}S_2$ NWs [5], FeP nanorod array [33] and Co-P/CC nanowire array [1], all effective in pH 14 (Table S1). The Tafel slope and exchange current density for Co-3Mo-B in alkaline media was calculated to be 67 mV/dec and 1.95 mA/cm^2 (Fig. 1c).

Fig. 1d shows the remarkable stability of Co-3Mo-B catalyst when tested under potentiostatic conditions in neutral and alkaline media for about 40 hours. Recycling tests (Fig. 1e-f) also show negligible loss in activity of Co-3Mo-B catalyst, even after 5000 cycles of operations in both neutral and alkaline solutions. These tests demonstrate excellent electrochemical stability of Co-3Mo-B in both the reaction media.

In order to understand the reasons for excellent catalytic behaviour, Co-3Mo-B was characterized by various techniques. From SEM image of Co-B and Co-3Mo-B NPs (Fig. S2), it is seen that Co-B NPs are highly agglomerated as compared to Co-3Mo-B. TEM image in Fig.2a gives better insight into the morphology of Co-3Mo-B NPs showing uniformly sized spherical NPs which are well separated and highly dispersed. From the corresponding histograms (inset of Fig.2a), a narrow size distribution of Co-3Mo-B NPs with average size of about 18 nm ± 6 nm, lower than that of Co-B (~ 30 nm) is observed (Fig. S3). Thus, inclusion

of a small amount of Mo in Co-B synthesis procedure leads to a considerable change in particle size and dispersion creating smaller sized NPs with uniform distribution: conditions favourable for catalytic processes.

The amorphous structure of Co-B NPs is well known, as also reported in our previous work [18, 20]. PXRD pattern of Co-3Mo-B (Fig. S4), shows the absence of any long- range ordering, as was the case in Co-B. However, on probing the local structure of these NPs at a higher magnification using HRTEM, the presence of some short-range ordering in the form of nano-sized crystalline domains surrounded by amorphous phase was observed. HRTEM image of a representative Co-3Mo-B NP is shown in Fig.2b. One could observe that Co-3Mo-B NP is not completely amorphous but also consists of small domains showing lattice fringes with d-spacings of 1.97 Å and 1.77 Å that corresponds to (211) planes of Co_2B phase as well as (303) planes of Co-hcp phase, respectively. These crystallographic domains are separated by grain boundaries, containing atoms with lower co-ordination number as compared to atoms in the ideal crystallites, making them highly active catalytic sites, which results in enhancing the catalytic activity. The polycrystalline nature of Co-3Mo-B NPs was also confirmed by SAED pattern (Fig.2c) which shows the diffraction spots in addition to the diffused rings. Thus, it becomes clearly evident that Co-3Mo-B NPs lack any long-range ordering and possess only short-range ordering owing to the presence of nano-sized crystalline domains. Fig.2 (d-f) shows scanning TEM (STEM) image and corresponding EDX elemental mapping images of Co and Mo in Co-3Mo-B, revealing a homogeneous distribution of Co and Mo in the sample. EDX spectra (Fig. S5) also confirmed the composition of Co and Mo in Co-3Mo-B catalyst. The presence of B, however, could not be established owing to the limitations of these techniques. Nevertheless, XPS was used to establish the surface elemental composition, including that of boron (Table S2). Fig.3 (a-c) shows XPS spectra of Co-3Mo-B

catalyst. The two peaks of Co $2p_{3/2}$ levels at BE of 777.9 eV and 781.3 eV were observed corresponding to metallic and oxidized cobalt. Similarly, two peaks for B1s level with BE of 187.7 eV and 191.9 eV were observed indicating the presence of metallic and oxidized boron in the sample. Elemental boron peak (187.7 eV) is positively shifted by about 0.7 eV as compared to that of pure B (187.0 eV). This shift results due to the phenomena of reverse electron transfer from B to Co atoms, typical of amorphous transition metal borides [18-21]. The BE peaks of Co $2p_{3/2}$ and B1s levels in Co-3Mo-B are consistent with that of Co-B catalyst and do not show any variation in presence of Mo. The XPS spectra of Mo 3d levels (Fig.3c), indicate that Mo is present only in oxidized state with BE peaks at 230.6, 232.3 and 233.6 eV corresponding to $3d_{5/2}$ levels of Mo. The BE peak at 232.3 eV is assigned to Mo^{4+} state whereas peak at 233.6 eV is assigned to Mo^{6+} state corresponding to $3d_{5/2}$ level of Mo.

It is concluded from the XPS data that the addition of Mo does not alter the electronic properties of Co-B. From the morphological analysis discussed above, it seems that the addition of Mo, leads to the formation of well-dispersed NPs with uniform size distribution, unlike Co-B. Based on these observations, we propose that in the present case, Mo (in oxidized form) acts like a barrier which prevents Co-B NPs from agglomeration. To confirm this, BET measurements were carried out and the corresponding isotherms are shown in Fig. 3(d-e). The BET surface area for Co-3Mo-B NPs was measured to be 38.8 ± 0.5 m^2/g which is almost twice the value measured for Co-B (20.3± 0.3 m^2/g). In both the cases, the same amount of Co-B was used. Most importantly, BET adsorption-desorption isotherms displayed a prominent hysteresis for Co-3Mo-B which is not visible for Co-B. The capillary action of the adsorbed layer is responsible for this hysteresis effect which is representative of Type H3 isotherms indicating mesoporous structure in Co-3Mo-B. This confirms the enhancement in specific surface area of the catalyst by the addition of Mo, to produce more

active sites for electrocatalysis. Here, it must be noted that the BET surface area increases further with increasing the Mo/(Mo+Co) ratio in Co-Mo-B. However, increasing the content of Mo implies reduction in the content or surface screening of active Co atoms, which in turn leads to a decline in the overall activity, as evident from Fig. S1.

To confirm the results derived from BET analysis, the electrochemical surface area (ESA) was estimated by measuring the double layer capacitance formed at the electrode/electrolyte interface. Cyclic voltammetry (CV) measurements were carried out in 0.1 M Na_2SO_4 solution [19] in the potential window of 100 mV on either sides of the open-circuit potential (OCP), so that no Faradaic processes are involved and the current response is only due to the charging of the double layer. Fig.3f (inset) shows a representative CV curve for Co-3Mo-B catalyst while those for Co-B and bare GC are reported in ESI (Fig. S6). ESA for Co-3Mo-B, based on the C_{dl} value(0.761 mF/cm^2), is 1.6 and 15 times higher than that of Co-B (0.481 mF/cm^2) and bare GC electrode (0.049 mF/cm^2), respectively. The increase in ESA of Co-3Mo-B is in accordance with the enhancement in specific surface area obtained by BET analysis, resulting in higher electrochemical performance of Co-3Mo-B.

To quantify the performance of a catalyst, it becomes crucial to probe the intrinsic catalytic activity obtained per active site, which can be estimated by calculating the turn-over frequency (TOF). Following a previously reported method [20], TOF value for Co-3Mo-B was calculated to be 0.0595atom^{-1}s^{-1} at an overpotential of 200 mV, in pH 7. This value is not only higher than that for Co-B but also higher than that for CoS film [4] and H_2 Co-cat [30], for all the analyses made at pH 7 (Table S3). Thus, the synergic effect created in Co-B with the addition of Mo to obtain Co-3Mo-B, not only increases the number of surface active sites, but also improves the HER activity per catalytic site. This improvement in the activity

of each site is attributed to the presence of nano-domains in each NPs, separated by grain boundaries having under-co-ordinated active atoms.

Motivated by the report on bifunctional nature of Co_2B-500 catalyst [21], we tested Co-3Mo-B for oxygen evolution reaction (OER) in 1 M NaOH solution. As speculated, Co-3Mo-B displayed superior performance for oxygen evolution as well, overhauling the report made for Co_2B-500 [21]. Fig.4a shows the anodic linear sweep curves for Co-3Mo-B catalyst in pH 14, along with that of RuO_2 catalyst loaded on GC for comparison. Co-3Mo-B requires an overpotential of 320 mV to attain 10 mA/cm^2 which is lower than that reported for Co_2B-500 (380 mV) [21], NG-CoSe/GC (370 mV) [34], Co/C/GC (390 mV) [35], Co_3O_4/NF (330 mV) [36],Ni/NiO(OH)/NC(390 mV) [37],$Ni_{0.9}Fe_{0.1}$/NC (330 mV) [38], CoP NR/C (340 mV) [39] and $MnNi_xO_y$ (430 mV) [40].RuO_2/GC could achieve the same current density at 270 mV. The Tafel slope analysis for Co-3Mo-B, yielded a value of 155 mV/dec (inset of Fig. 4a).Co-3Mo-B showed favourable recycling behaviour with a marginal decrease in OER activity after 1000 cycles (Fig. 4b). It also showed high stability for about 10 hours of OER operation at a constant overpotential of 350 mV (inset of Fig. 4b). The test for OER was also performed in pH 7 solution, however the potential required to drive the current densities were on higher side (2.03 V for 10 mA/cm^2) as shown in Fig. S7.

The mechanism for oxygen evolution in alkaline media initiates with the adsorption of OH^- ions on the electrode surface [16]. In alkaline media, the Mo oxide in Co-3Mo-Bplays the role of a Lewis acid site and readily attracts OH^- ions (Lewis base) toward the electrode surface, thereby initiating OER process more efficiently. The adsorbed OH then reacts with other OH^- ions leading to the formation of an intermediate oxide/hydroxide layer. The final step involves the interaction of OH^- ions with this oxide/hydroxide layer to form O_2 molecule

which is later desorbed from the electrode surface. It has been reported numerous times that the formation of these oxide/hydroxide type species on the electrode surface plays a vital role in improving the oxygen evolution rate [14, 15, 21]. Fig.S9 shows the XPS spectrum of Co 2p levels in Co-3Mo-B electrode after testing it for OER in pH 14 for about 50 cycles. We see that the peak corresponding to metallic Co vanishes and two peaks are observed for Co $2p_{3/2}$ levels at BE of 780.1 eV and 781.3 eV, corresponding to the formation of Co(OH)O and $Co(OH)_2$ species. As discussed above, these species are active for OER and the appearance of these on the surface of Co-3Mo-B explains its effectiveness for OER. The XPS spectra for B 1s and Mo 3d levels showed no variation from their initial forms. As a test of bifunctional nature, Co-3Mo-B was tested in alkaline medium by sweeping the potential from cathodic region to anodic region and the corresponding graph is shown in Fig.4c. From the figure, it could be seen that Co-3Mo-B shows true bifunctional character, producing H_2 and O_2 efficiently, in the respective potential regions.

Once the bifunctional nature of Co-3Mo-B is established, its practical use can be demonstrated by using it as both cathode and anode in a 2-electrode electrolysis system. For the sake of comparison, a similar experiment was carried out where Pt served as the hydrogen evolving catalyst and RuO_2 was used as the oxygen evolving electrode , in an alkaline medium. From Fig.4d, one could see that this 2-electrode alkaline electrolysis assembly could produce 10 mA/cm^2 at a cell voltage of 1.69 V for Co-3Mo-B || Co-3Mo-B, which is higher than that for RuO2|| Pt (1.52V but lower than that reported for Co_2B-500 || Co_2B-500/NG (1.81 V) [21] and comparable to NiP/NF || NiP/NF (1.67 V) [13], FeP NTs || FeP NTs (1.69 V) [14], CoSe/Ti || CoSe/Ti (1.65 V) [15] and other totally non-noble electrocatalysts (Table S4). In this 2-electrode assembly, Co-3Mo-B could maintain a

constant current density at 1.69 V for about 25 hours of full water electrolysis (inset of Fig. 4d), making it highly attractive for industrial applications.

Conclusion:

In summary, we have shown that Co-3Mo-B nanocatalyst, synthesized by a facile reduction reaction, is an efficient catalyst for HER in neutral and alkaline media. The enhancement in activity of Co-3Mo-B was attributed to the synergic effect created by the addition of Mo in Co-B, leading to an increase in the effective surface area and also improvement in the activity per catalytic site. Co-3Mo-B also turned out to be an efficient catalyst for oxygen evolution, owing to the formation of oxide/hydroxide species of Co on its surface, in alkaline medium. The bifunctional characteristic of Co-3Mo-B was explored by employing it as both electrodes in a 2-electrode cell where it could generate 10 mA/cm^2 at an operating voltage of 1.69 V, in an alkaline medium, with high stability. It is worth mentioning that, to the authors' best knowledge, the present Co-3Mo-B stands out as the most superior bifunctional metal boride electrocatalyst reported so far. It also presents favourable conditions of further improvement by nanostructuring or using suitable conducting supports. We finally expect that these results would stimulate increased research activity for transition-metal borides as inexpensive electrocatalysts for full water splitting.

Supporting Information:

Additional experimental details, chemicals and materials, TOF calculations, additional SEM, TEM, EDX, XRD, XPS and electrochemical data, HER and OER comparison tables..

Acknowledgements:

The research activity is partially supported by UGC-UPE Green Technology Project, India and

PAT (ProvinciaAutonoma di Trento) project ENAM in co-operation with Istituto PCB of CNR (Italy). R. Fernandes and N. Patel acknowledges UGC for providing financial support through Dr. D. S. Kothari postdoctoral fellowship program and Faculty recharge program respectively. We thank Saloni Sharma for TEM analysis, Sushmita Bhartiya and P K Gupta for BET measurements.

References:

1. Tian, J.; Liu, Q.; Asiri, A. M.; Sun, X. *J. Am. Chem. Soc.***2014**, 136,7587–7590.
2. Popczun, E. J.; Read, C. G.; Roske, C. W.; Lewis, N. S.; Schaak, R. E. *Angew. Chem.***2014**, 126, 5531–5534.
3. Callejas, J. F.; McEnaney, J. M.; Read, C. G.; Crompton, J. C.; Biacchi, A. J.; Popczun, E. J.; Gordon, T. R.; Lewis, N. S.; Schaak, R. E. *ACS Nano***2014**, 8, 11101-11107.
4. Sun, Y.; Liu, C.; Grauer, D. C.; Yano, J.; Long, J. R.; Yang, P.; Chang, C. J. *J. Am. Chem. Soc.***2013**, 135, 17699−17702.
5. Peng, Z.; Jia, D.; Al-Enizi, A.; Elzatahry, M. A. A.; Zheng, G. *Adv. Energy Mater.***2015**, 5, 1402031.
6. Wang, K.; Xi, D.; Zhou, C.; Shi, Z.; Xia, H.; Liu, G.; Qiao, G. *J. Mater. Chem. A***2015**, 3, 9415-9420.
7. Zou, M.; Chen, J.; Xiao, L.; Zhu, H.; Yang, T.; Zhang, M.; Du, M. *J. Mater. Chem. A***2015**, 3, 18090-18097.
8. Liu, Y.; Yu, G.; Li, G. D.; Sun, Y.; Asefa, T.; Chen, W.; Zou, X. *Angew. Chem. Int. Ed.***2015**, 54, 1-6.
9. Vrubel, H.; Hu, X. *Angew. Chem. Int. Ed.***2012**, 51, 12703 –12706.
10. Liang, H. W.; Bruller, S.; Dong, R.; Zhang, J.; Feng, X.; Mullen, K. *Nat. Comm.***2015**, 6.
11. Chen, L.; Wang, M.; Han, K.; Zhang, P.; Gloaguen, F.; Sun, L. *Energy Environ. Sci.***2014**, 7, 329–334.
12. Zeng, M.; Li, Y. *J. Mater. Chem. A***2015**, 3, 14942-14962.
13. Tang, C.; Asiri, A. M.; Luo, Y.; Sun, X. *ChemNanoMat***2015**, 1, 558-561.
14. Yan, Y.; Xia, B. Y.; Ge, X.; Liu, Z.; Fisher, A.; Wang, X. *Chem. Eur. J.***2015**, 21, 1-7.
15. Liu, T.; Liu, Q.; Asiri, A. M.; Luo, Y.; Sun, X. *Chem. Commun.***2015**, 51, 16683-16686.
16. Zhu, Y. P.; Liu, Y. P.; Ren, T. Z.; Yuan, Z. Y. *Adv. Funct. Mater.***2015**, 25, 7337-7347.
17. Zhang, Z.; Hao, J.; Yang, W.; Tang, J. *RSC Adv.* **2016**, 6, 9647-9655.
18. Gupta, S.; Patel, N.; Miotello, A.; Kothari, D. C.; *J. Power Sources***2015**, 279, 620-625.
19. Zhang, P.; Wang, M.; Yang, Y.; Yao, T.; Han, H.; Sun, L. *Nano Energy***2016**, 19, 98-107.
20. Gupta, S.; Patel, N.; Fernandes, R.; Kadrekar, R.; Dashora, A.; Yadav, A. K.; Bhattacharyya, D.; Jha, S. N.; Miotello, A.; Kothari, D. C. *Appl. Cat. B: Environ.***2016**, 192, 126-133.
21. Masa, J.; Weide, P.; Peeters, D.; Sinev, I.; Xia, W.; Sun, Z.; Somsen, C.; Muhler, M.; Schuhmann, W. *Adv. Energy Mater.***2016**, 1502313.

22. Wang, D.; Zhang, D.; Tang, C.; Zhou, P.; Wu, Z.; Fang, B. *Catal. Sci. Technol.***2016**, 6, 1952-1956.
23. Hao, J.; Yang, W.; Zhang, Z.; Tang. J. *Nanoscale***2015**, 7, 11055-11062.
24. Staszak-Jirkovský, J.; Malliakas, C. D.; Lopes, P. P.; Danilovic, N.; Kota, S. S.; Chang, K. C.; Genorio, B.; Strmcnik, D.; Stamenkovic, V. R.; Kanatzidis, M. G.; Markovic, N. M. *Nat. Mater.* **2016**, 15, 197-203.
25. Zhang, H.; Li, Y.; Xu, T.; Wang, J.; Huo, Z.; Wana P.; Sun, X. *J. Mater. Chem. A***2015**, 3, 15020-15023.
26. Sarkar, S.; Sampath, S. *Chem. Comm.***2014**, 50, 7359—7362.
27. Liu, X.; Cui, S.; Sun, Z.; Du, P. *Chem. Comm.***2015**, 51, 12954-12957.
28. Pu, Z.; Liu, Q.; Asiri, A. M.; Sun, X. *ACS Appl. Mater. Interfaces***2014**, 6, 21874-21879.
29. Tian, J.; Liu, Q.; Liang, Y.; Xing, Z.; Asiri, A. M.; Sun, X. *ACS Appl. Mater. Interfaces***2014**, 6, 20579-20584.
30. Cobo, S.; Heidkamp, J.; Jacques, P.; Fize, J.; Fourmond, V.; Guetaz, L.; Jousselme, B.; Ivanova, V.; Dau, H.; Palacin, S.; Fontecave, M.; Artero, V. *Nat. Mater.***2012**, 11, 802-807.
31. Gong, M.; Zhou, W.; Tsai, M. C.; Zhou, J.; Guan, M.; Lin, M. C.; Zhang, B.; Hu, Y.; Wang, D. Y.; Yang, J.; Pennycook, S. J.; Hwang, B. J.; Dai, H. *Nat. Comm.***2014**, 5, 1-6.
32. Zhang, K.; Zhao, Y.; Fu, D.; Chen, Y. *J. Mater. Chem. A***2015**, 3, 5783-5788.
33. Liang, Y.; Liu, Q.; Asiri, A. M.; Sun, X.; Luo, Y. *ACS Catal.* **2014**, 4, 4065-4069.
34. Gao, M. R.; Cao, X.; Gao, Q.; Xu, Y. F.; Zheng, Y. R.; Jiang, J.; Yu, S. H. *ACS Nano***2014**, 8, 3970–3978.
35. Wu, L.; Li, Q.; Wu, C. H.; Zhu, H.; Mendoza-Garcia, A.; Shen, B.; Guo, J.; Sun, S. *J. Am. Chem. Soc.***2015**, 137, 7071–7074.
36. Esswein, A. J.; McMurdo, M. J.; Ross, P. N.; Bell, A. T.; Tilley, T. D. *J. Phys. Chem. C***2009**, 113, 15068–15072.
37. Ren, J.; Antonietti, M.; Fellinger, T. P. *Adv. Energy Mater.***2015**, 5, 1401660.
38. Zhang, X.; Xu, H.; Li, X.; Li, Y.; Yang, T.; Liang, Y. *ACS Catal.***2016**, 6, 580−588.
39. Chang, J.; Xiao, Y.; Xiao, M.; Ge, J.; Liu, C.; Xing, W. *ACS Catal.***2015**, 5, 6874−6878.
40. Ledendecker, M.; Clavel, G.; Antonietti, M.; Shalom, M. *Adv. Func. Mater.***2015**,25, 393-399.

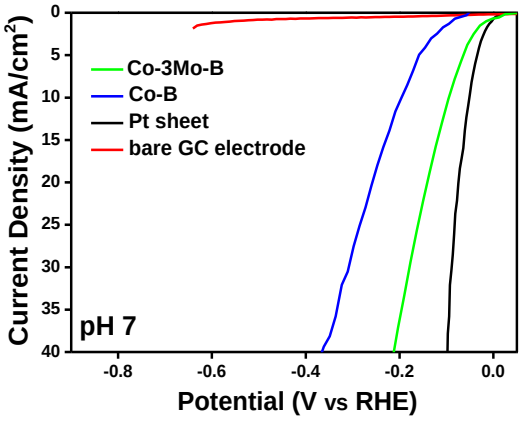

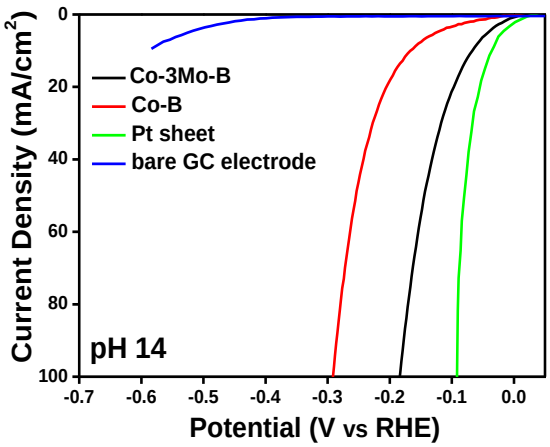

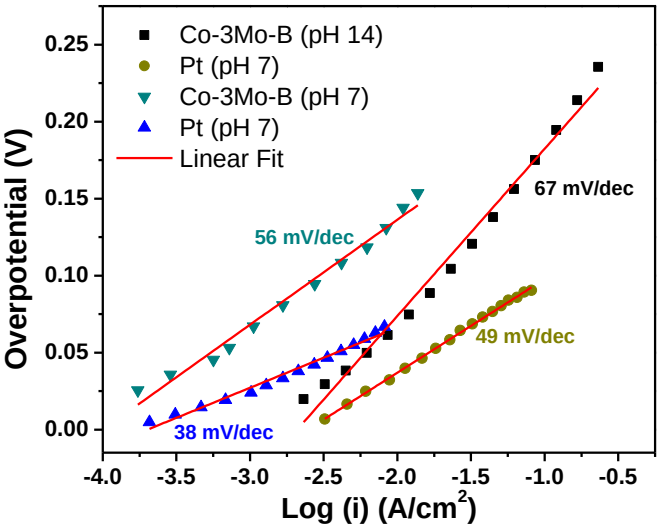

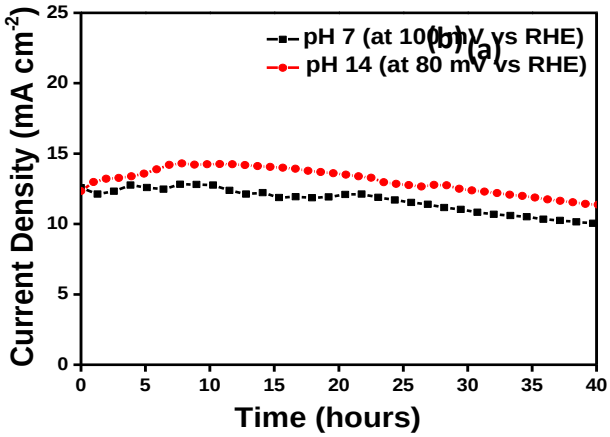

(c)

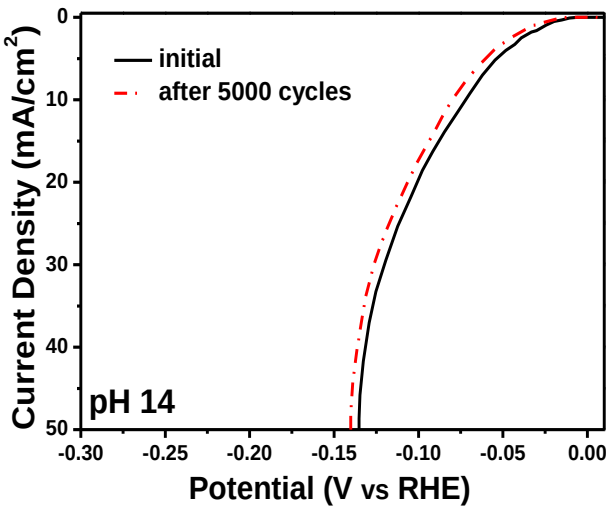

Fig. 1 Linear polarization curves **(a)** in pH 7; **(b)** in pH 14 and **(c)**Tafel plots for Pt electrode, Co-3Mo-B, Co-B and bare GC

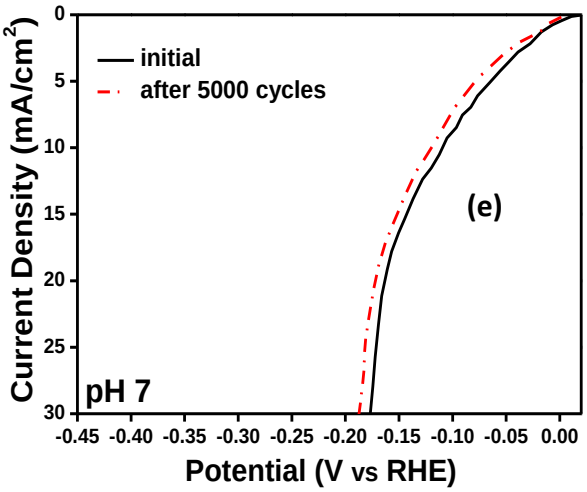

electrode; **(d)** Time-dependent potentiostatic curves for Co-3Mo-B catalyst at 100 mV in pH 7 and 80 mV in pH 14; Linear polarization curves of Co-3Mo-B before and after 5000 cycles in **(e)**0.5 MKPi (pH 7) and **(f)**1 M NaOH (pH 14) (at a scan rate of 100 mV/s).

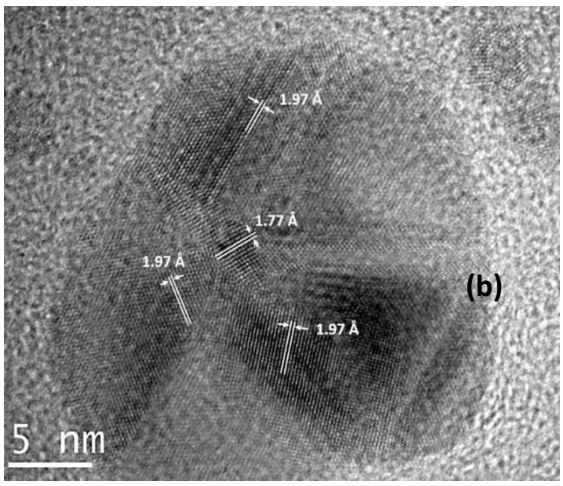

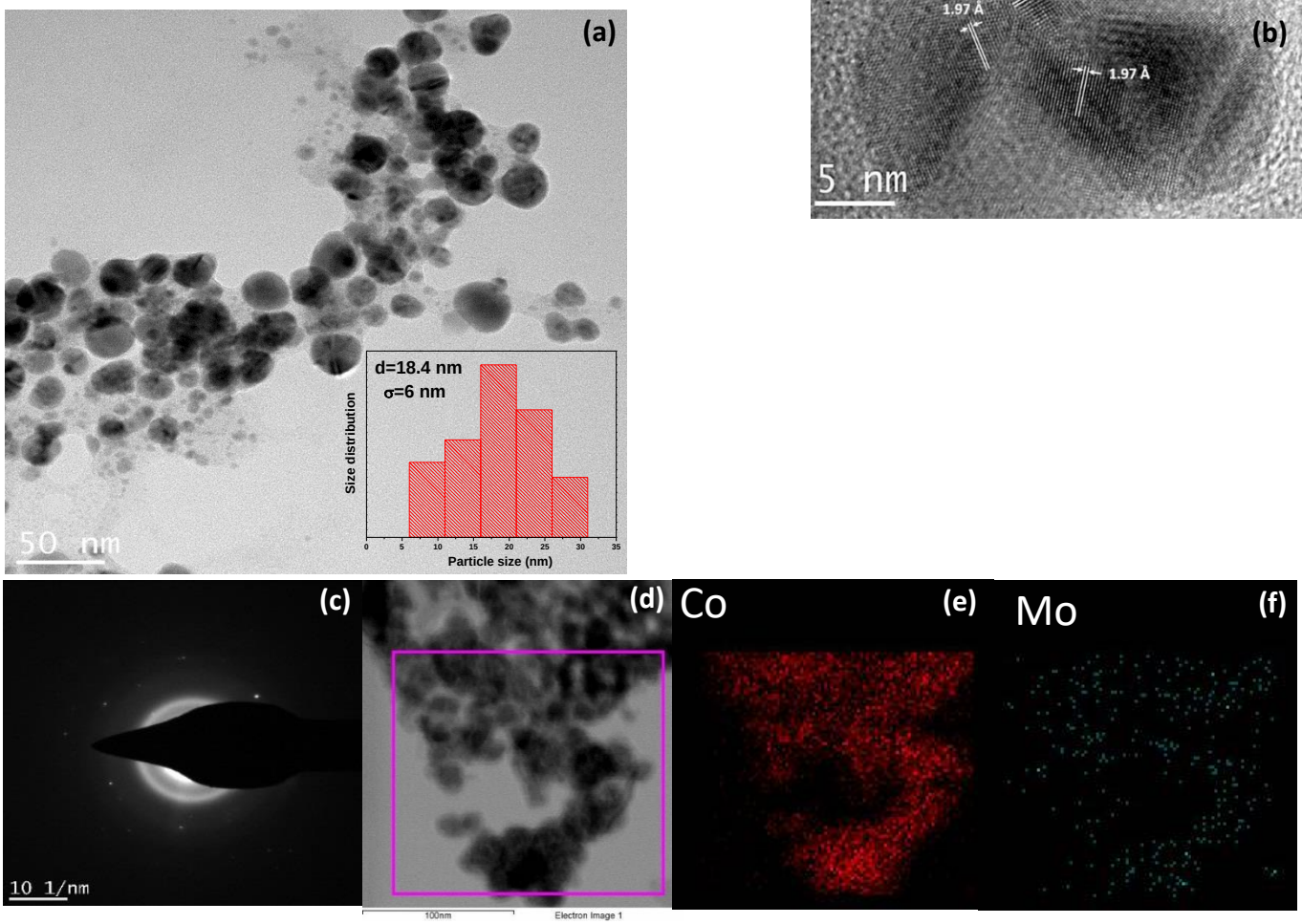

Fig. 2(a) Bright field TEM image of Co-3Mo-B catalyst powder with size distribution (inset); **(b)**HRTEM image of a representative Co-3Mo-B nanoparticle; **(c)**SAED pattern of Co-3Mo-B showing polycrystalline nature; **(d –f)**Scanning TEM (STEM) image and corresponding EDX elemental mapping images of Co and Mo in Co-3Mo-B.

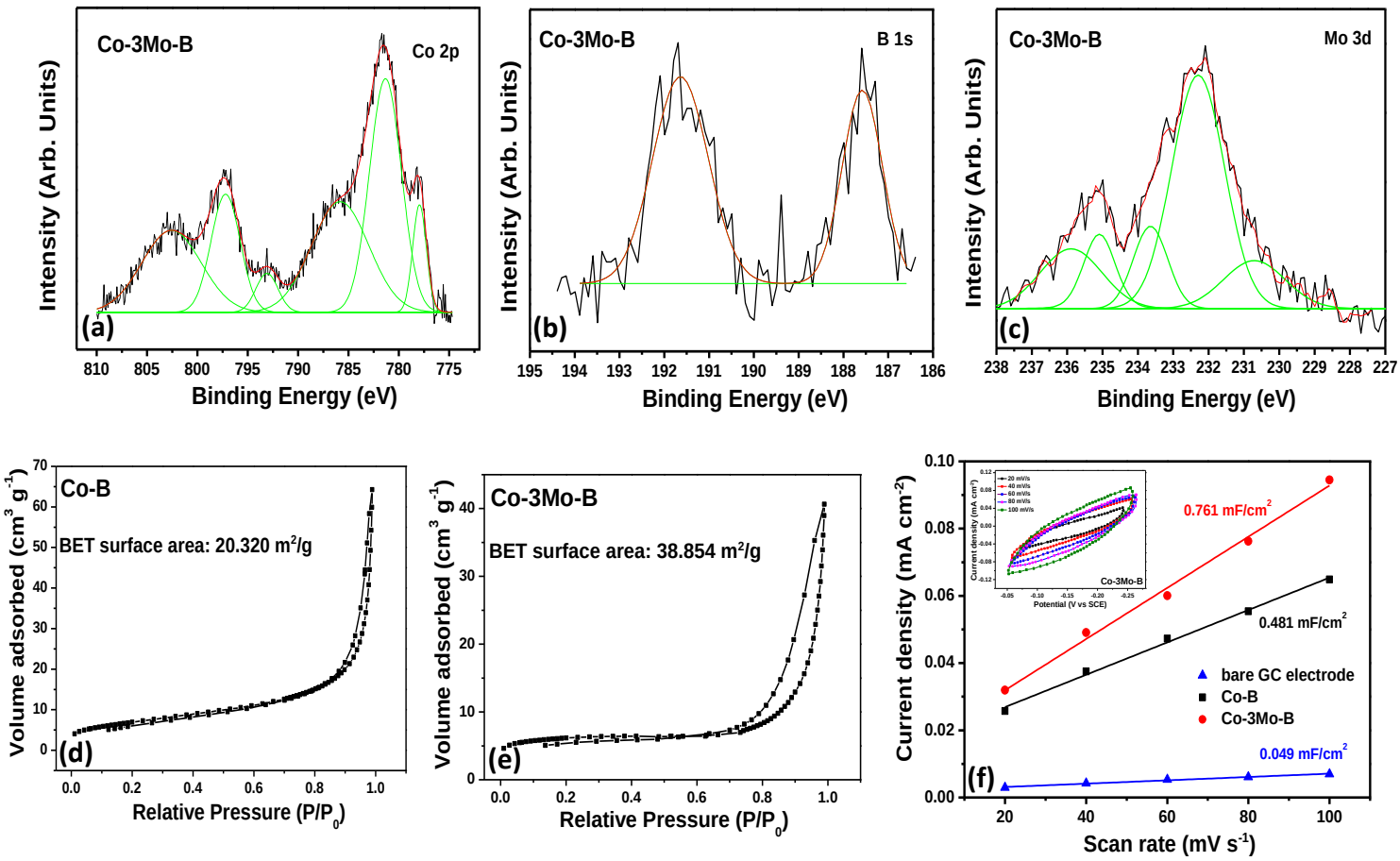

Fig. 3(a-c)XPS spectra of Co 2p, B 1s and Mo 3d states in Co-3Mo-B; BET adsorption-desorption isotherms for**(d)** Co-B and **(e)** Co-3Mo-B; **(f)**Cyclic voltammogram for Co-3Mo-B catalyst (inset) at different scan rates from 20 to 100 mV/s and the measured capacitive currents plotted as a function of scan rate.

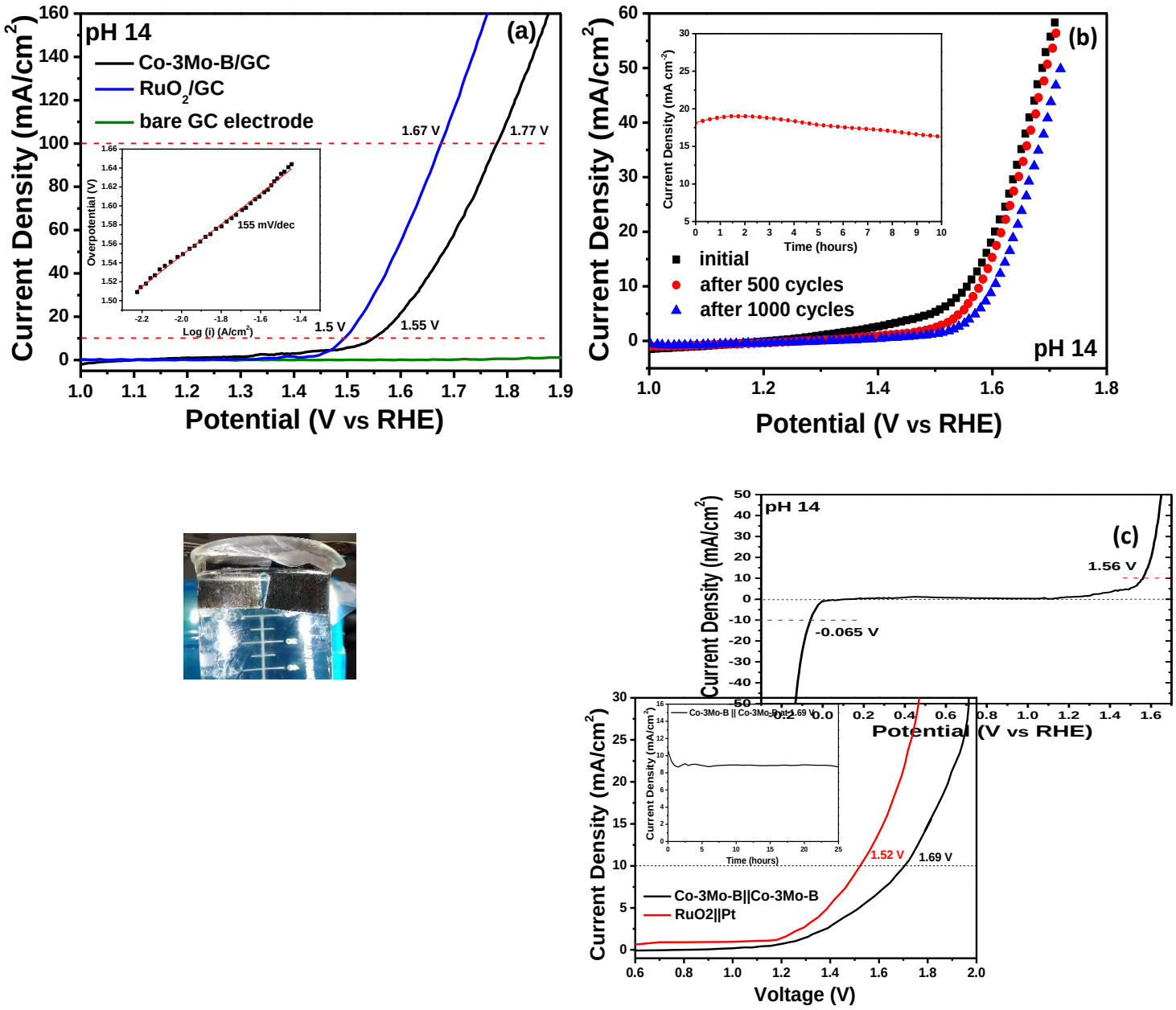

Fig. 4: (a) Anodic linear polarization curves for RuO_2 electrode, Co-3Mo-B and bare GC electrode in pH 14; **(b)**Recycling and stability curves (inset) for Co-3Mo-B catalyst in pH 14; **(c)** LSV curve for Co-3Mo-B showing its ability to function both as a HER catalyst as well as an OER catalyst in pH 14; **(d)**Polarization curves for Co-30Mo-B||Co-30Mo-B and RuO_2||Pt for overall water splitting in 1 M NaOH (2-electrode assembly) while inset shows potentiostatic water electrolysis at1.69 V for Co-30Mo-B||Co-30Mo-B over 25 hours.

Graphical Abstract

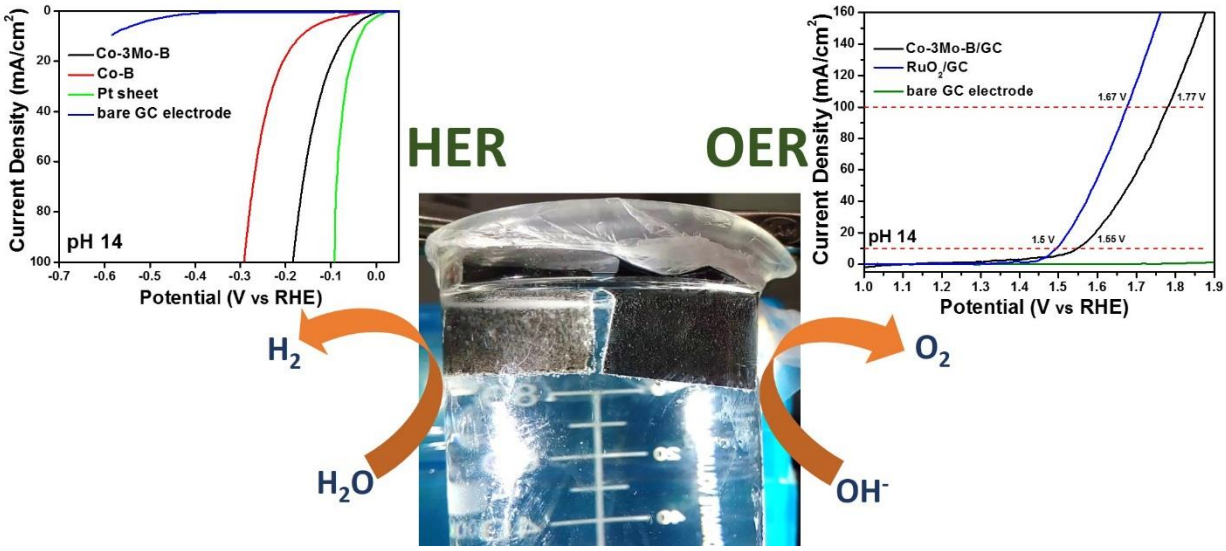

Supporting Information

for

Co-Mo-B Nanoparticles as a non-precious and Efficient Bifunctional Electrocatalyst for Hydrogen and Oxygen Evolution

S.Gupta[a*], N.Patel[a*], R.Fernandes[a], S.Hanchate[a], A.Miotello[b] and D. C. Kothari[a]

[a]Department of Physics and National Centre for Nanosciences & Nanotechnology, University of Mumbai, Vidyanagari, Santacruz (E), Mumbai 400098, India.

[b]Dipartimento di Fisica, Università degli Studi di Trento, I-38123 Povo (Trento), Italy.

Additional ExperimentalDetails:

Chemicals and Materials:

Cobalt chloride hexahydrate [$CoCl_2.6H_2O$, 99%] (SDFCL),sodium molybdatedihydrate [$Na_2MoO_4.2H_2O$, 99%](SDFCL), and sodium borohydride [$NaBH_4$, 98%] (SDFCL) were used for synthesizing the catalysts. Sodium hydroxide [NaOH, 98%] (Merck), di-potassium hydrogen orthophosphate [K_2HPO_4, 99%] (SDFCL), potassium dihydrogen orthophosphate [KH_2PO_4, 99.5%] (SDFCL), sodium sulphate [Na_2SO_4, 99.5%] (SDFCL) were used to prepare the electrolytic solutions. Double distilled water (DDW) was used for all practical purposes.

Preparation of electrolytes:

1 M NaOH and0.5 M potassium phosphate buffer (KPi) were used as electrolytes for all the electrochemical measurements at pH values of 14 and 7, respectively. For determination of ESA, 0.1 M Na_2SO_4 (pH 7) solution was used. Prior to their use, all the electrolyte solutions were purged with pure N_2 gas for about 20 min to remove dissolved oxygen.

Calculation of TOF values:

Molar mass of Co-3Mo-B = 130.897 g/mol

Density = 8.116 g/cm^3

Molar volume = 16.128 mL/mol

BET surface area: 388.5 cm^2/mg

Current density in pH 7 for a catalyst loading of 2.1 mg/cm^2:

At $\eta_{200\ mV}$: 36.15 mA/cm^2

Average surface atoms per 1 cm^2 of catalyst:

$$\left(\frac{3 * 6.022 * 10^{23}}{1\ mol} * \frac{1\ mol}{16.128\ cm^3}\right)^{2/3} = 2.3236 * 10^{15} atoms/cm^2$$

Surface atoms per testing area at 2.1 mg/cm^2:

$$\frac{2.1\ mg}{1\ cm^2\ (glassy\ carbon)} * \frac{388.5\ cm^2(catalyst)}{mg} * \frac{2.3236 * 10^{15} atoms}{1\ cm^2(catalyst)} = 1.895 * 10^{18} \frac{atoms}{test\ area}$$

Turnover frequency (per surface atom) at overpotential of 200 mV:

$$\frac{1\ turnover}{2\ e^-} * \frac{36.15 * 10^{-3} A}{1\ cm^2} * \frac{1\ mol}{96485\ C} * \frac{6.022 * 10^{23} e^-}{1\ mol} * \frac{1\ test\ area}{1.895 * 10^{18} atoms}$$

$$= \mathbf{0.0595\ s^{-1}}$$

Catalyst	**pH**	**J_o (mA/cm^2)**	**Onset (mV)**	**Overpotential (mV)**	**Tafel slope (mV/dec)**
Co-S film[1]	7	0.256	43	83 at 2 mA/cm^2	93
H_2-Cocat[2]	7	0.003	50	385 at 2 mA/cm^2	140
Co-P/CC nanowire array[3]	7	-	45	65 at 2 mA/cm^2 106 at 10 mA/cm^2	93
	14	-	80	209 at 10 mA/cm^2	129
Cu_2-Mo-S_4[4]	7	0.040	160	210 at 2 mA/cm^2	95
Co-P_4-N_2[5]	7	-	80	230 at 2 mA/cm^2	-
Co-P/Ti[6]	7	-	100	102 at 2 mA/cm^2 149 at 10 mA/cm^2	58
Fe-P/Ti[7]	7	-	100	200 at 10 mA/cm^2	99
Fe-P/Ti[8]	6.5	-	-	102 at 10 mA/cm^2	-
Fe-P/CC[9]	7	-	46	60 at 2 mA/cm^2 115 at 10 mA/cm^2	70

FePnanorod array[10]	7	-	112	202 at 10 mA/cm^2	71
	14	-	86	218 at 10 mA/cm^2	146
WP_2nanorods[10]	7	-	-	172 at 2 mA/cm^2 298 at 10 mA/cm^2	79
	14	-	-	225 at 10 mA/cm^2	84
W-P Nanoarrays on CC[12]	7	-	100	95 at 2 mA/cm^2 200 at 10 mA/cm^2	125
	14	-	-	150 at 10 mA/cm^2	102
W_2N Nanoarrays on CC[13]	7	-	-	186 at 2 mA/cm^2 302 at 10 mA/cm^2	182
	14	-	-	285 at 10 mA/cm^2	-
MoS_2/N-graphene aerogel[14]	7			167 at 5 mA/cm^2 261 at 10 mA/cm^2	230
NiS_2 nanosheets on CC[15]	7	-	150	193 at 2 mA/cm^2 243 at 10 mA/cm^2	69
	14	-	70	78 at 2 mA/cm^2 149 at 10 mA/cm^2	104
$Ni_{0.33}Co_{0.67}S_2$ Nanowires[16]	7	0.893	39	72 at 10 mA/cm^2 130 at 50 mA/cm^2	67.8
	14	-	50	88 at 10 mA/cm^2	118
CoS_2 Nanowires[16]	7	0.976	52.5	87 at 10 mA/cm^2	87.1
NiS_2 Nanoflakes[16]	7	0.643	77.6	187 at 10 mA/cm^2	105.1
C coated Co_9S_8 NPs[17]	7	-	-	150 at 1 mA/cm^2 280 at 10 mA/cm^2	-
	14	-	-	250 at 10 mA/cm^2	-
Cu(0) catalyst[18]	7	-	70	157 at 1 mA/cm^2	127
Mo_2C@NC[19]	7	-	-	156 at 10 mA/cm^2	-
	14		-	60 at 10 mA/cm^2	-
Mo_2C in N-doped CNTs[20]	7	-	-	645 at 10 mA/cm^2	-
	14	-	-	257 at 10 mA/cm^2	-
CoNx/C[21]	7	-	30	247 at 10 mA/cm^2	-
	14	-	30	170 at 10 mA/cm^2	-
NiO/Ni-CNT[22]	14			80 at 10 mA/cm^2	
Ni-Mo nanopowder[23]	14			70 at 10 mA/cm^2	
Ni_5P_4[24]	14			50 at 10 mA/cm^2	
Co NPs in NCarbon[25]	14			70 at 10 mA/cm^2	
Ni-Bx film[26]	7	0.851	77	54 at 10 mA/cm^2	
	14	0.275	88	135 at 10 mA/cm^2	
Co-30Ni-B[27]	7	0.708	53	170 at 10 mA/cm^2	51
	14		-	93 at 5 mA/cm^2 133 at 10 mA/cm^2	
Co-B*	**7**	**0.501**	**65**	**197 at 10 mA/cm^2**	**71**
	14			**166 at 10 mA/cm^2** **290 at 100 mA/cm^2**	

Co-3Mo-B*	**7**	**1.20**	**-**	**35 at 2 mA/cm^2** **96 at 10 mA/cm^2**	**56**
	14	**1.95**	**-**	**66 at 10 mA/cm^2** **184 at 100 mA/cm^2**	**67**

*** This work**

Table S1: Comparison of electrochemical parameters for HER between Co-3Mo-B catalyst and various solid-state catalysts active in neutral and alkalinemedia.

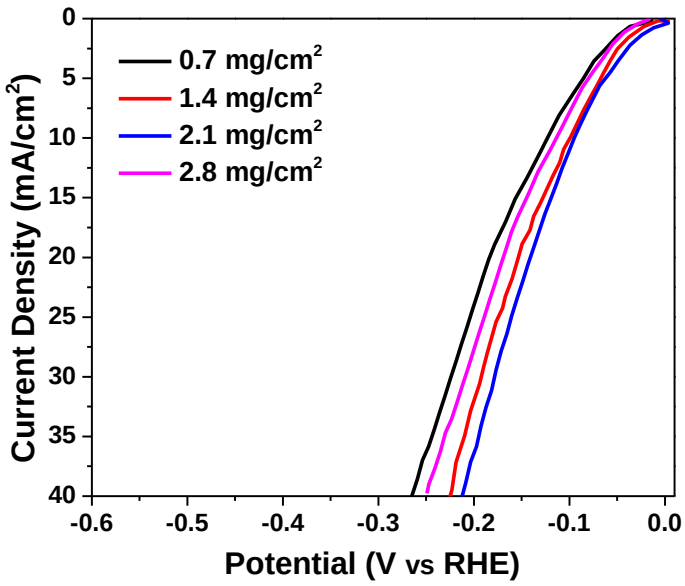

Figure S1: Linear polarization curves for HER on Co-3Mo-B catalyst with different mass-loading, in pH 7 phosphate buffer.

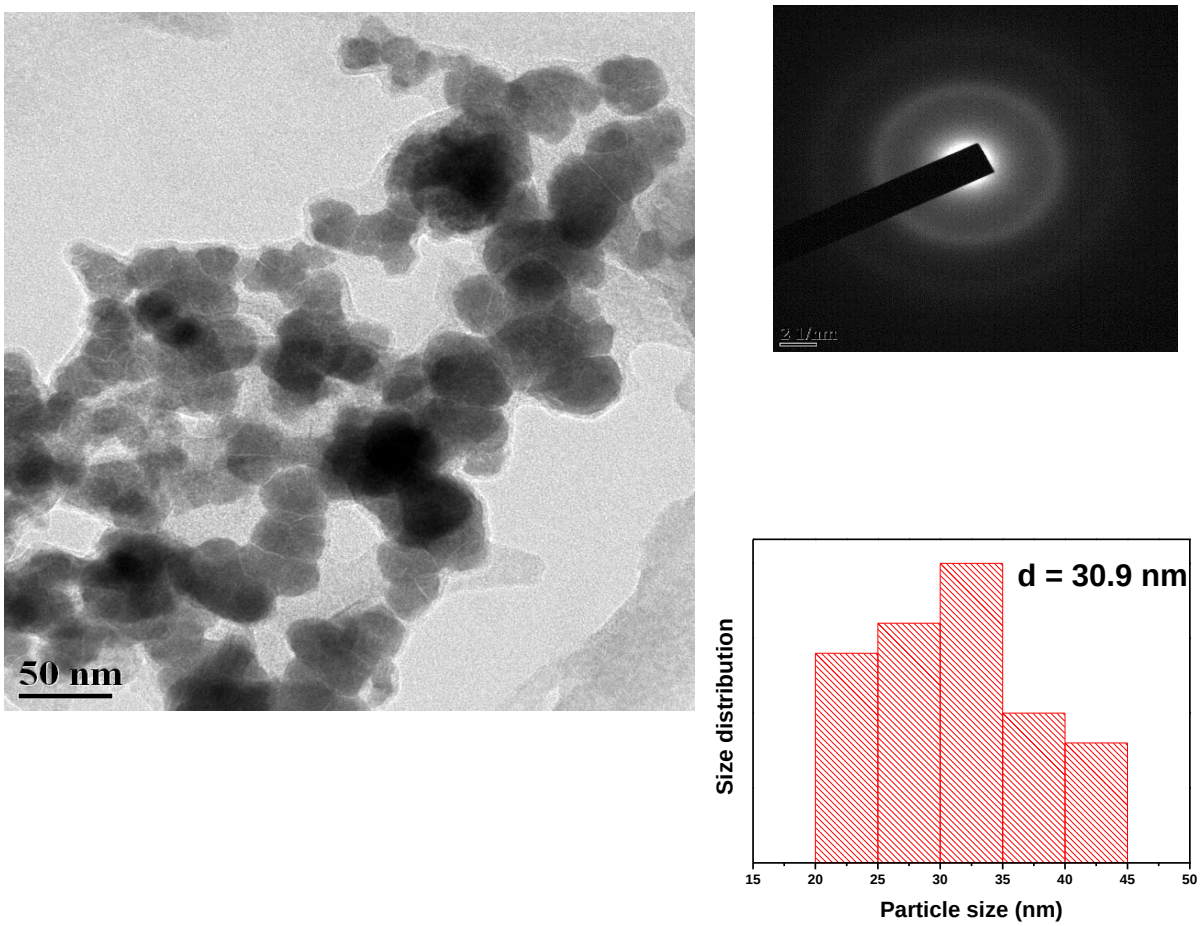

Figure S2: TEM image of Co-B powder with SAED pattern and size distribution histogram.

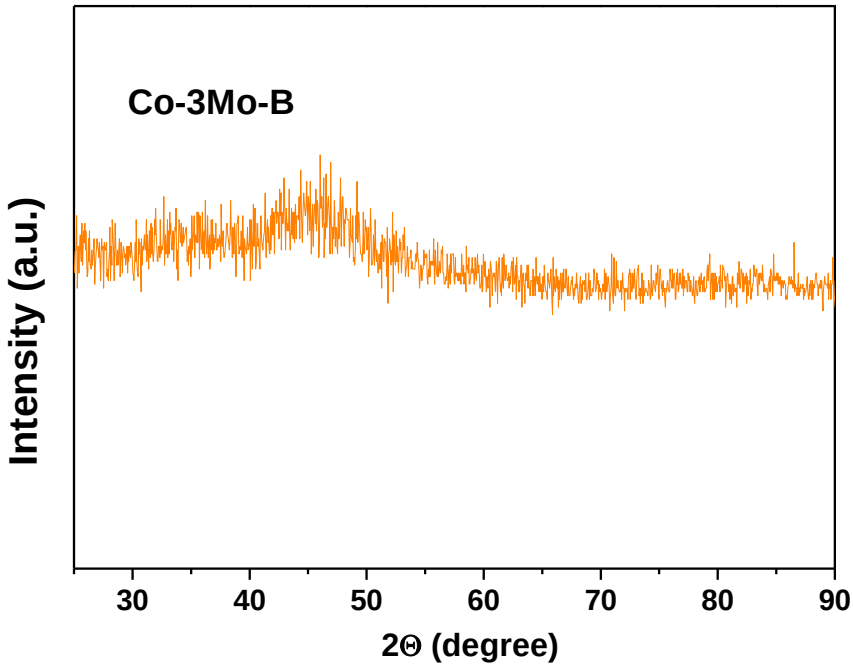

Figure S3: PXRD pattern of Co-3Mo-B nanoparticle showing amorphous structure.

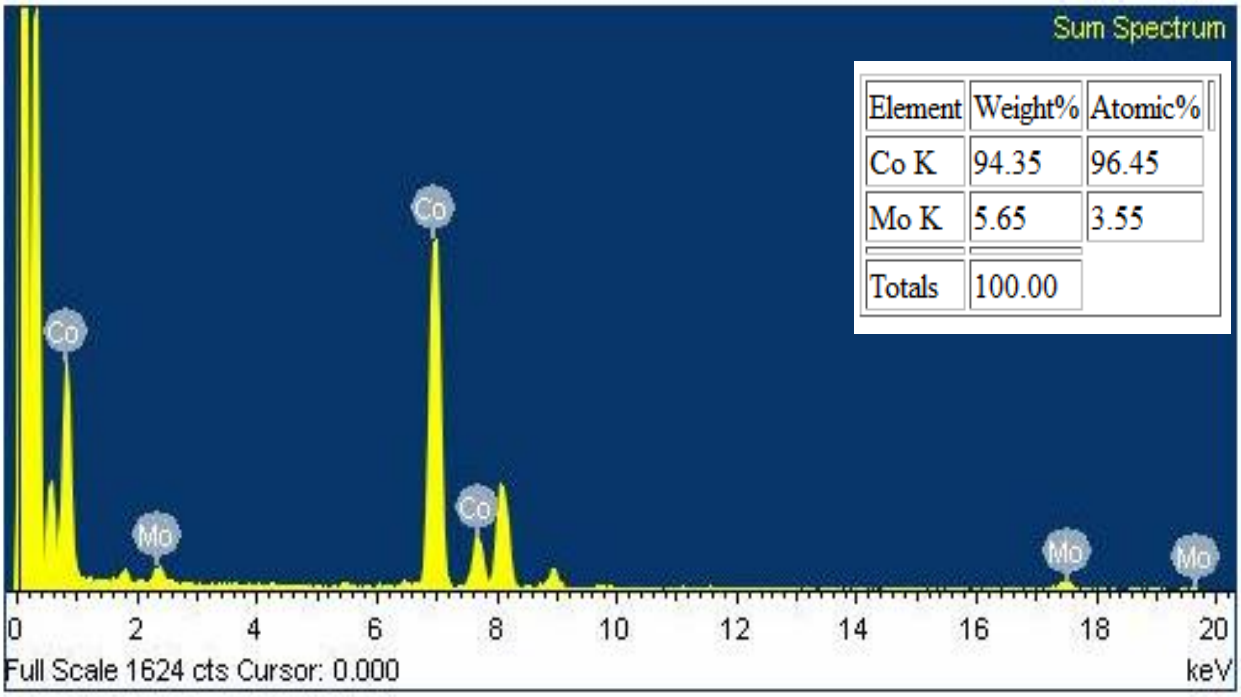

Figure S4: EDX spectrum of Co-3Mo-B nanocatalyst with respective compositions.

Sample	Peak Position (eV)					Concentration (Atomic %)		
	Co		Mo	B		Co	Mo	B
	Elemental	Oxide	Oxide	Elemental	Oxide			
Co-B	777.9	---	---	187.8		58	---	42
Co-3Mo-B	777.9	781.3	230.6, 232.3, 233.6, 235.1, 235.9	187.7	191.9	59.98	2.77	37.25

Table S2. Binding energy peak positions and percentage surface composition for Co-B and Co-3Mo-B catalysts obtained from XPS analysis.

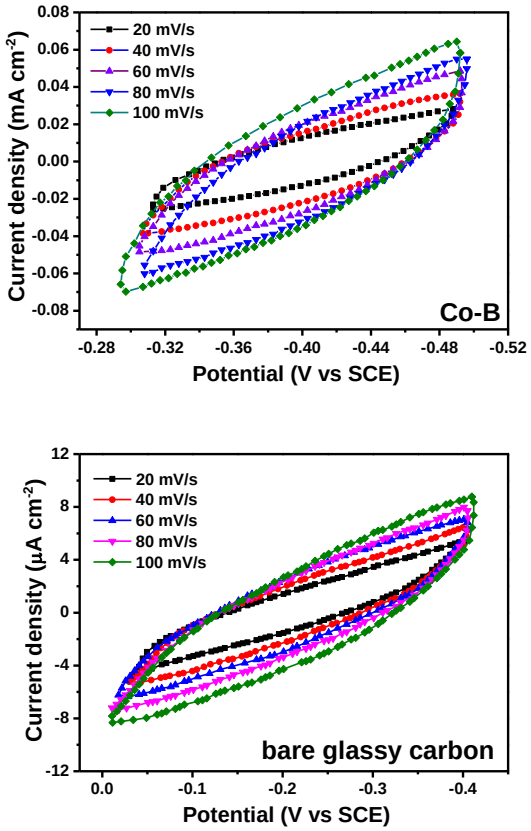

Figure S5: CV curves for Co-B and bare GC electrode in 0.1 M Na_2SO_4 solution to determine the double layer capacitance.

Catalyst	Overpotential (V vs RHE)	TOF (s^{-1})
Co-S film[1]	Not mentioned	0.017
H_2-Cocat[2]	0.385	0.022
MoS_3-CV film[28]	0.340	0.300
Co-30Ni-B[27]	0.200	0.062
Co-B	0.200	0.033
Co-3Mo-B	0.200	0.059

Table S3: Comparison of TOF values with other reports from literature in pH 7.

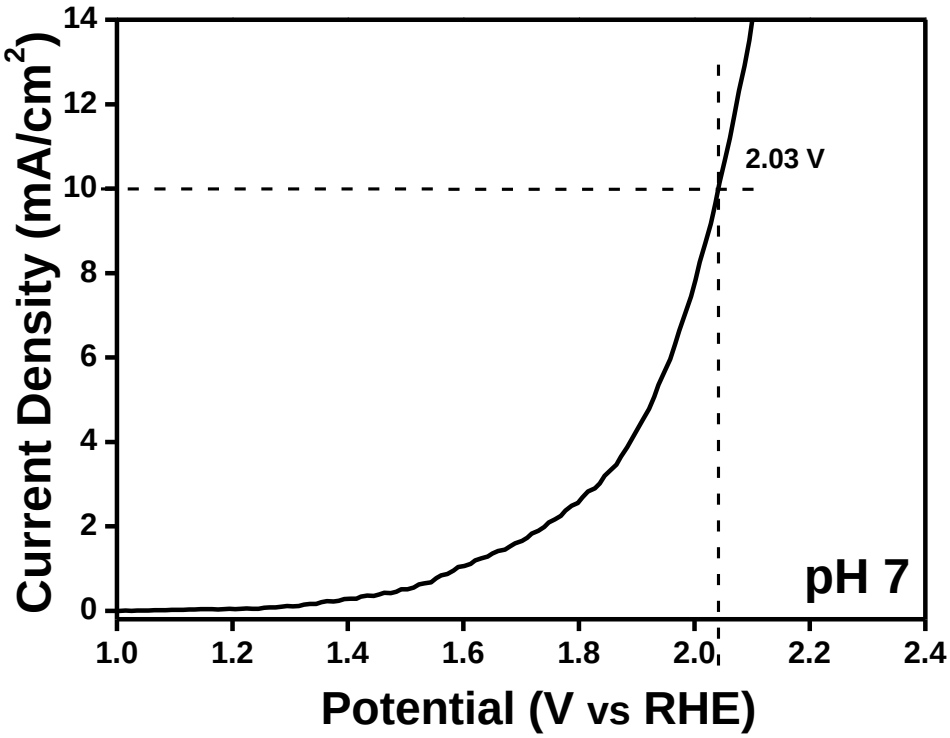

Figure S6: Anodic linear polarization curve for Co-3Mo-B catalyst in pH 7.

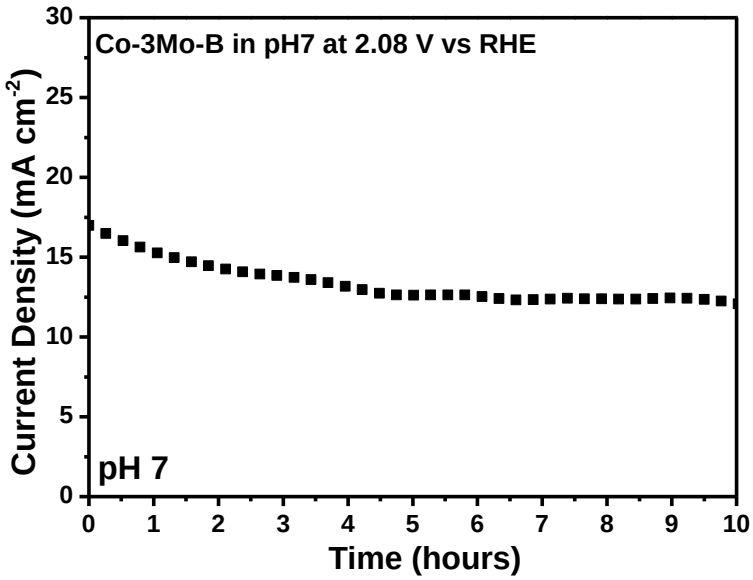

Figure S7: Potentiostatic curve for Co-3Mo-B catalyst in pH 7 at 2.08 V.

Catalyst	Overpotential (mVvs RHE) to achieve 10 mA/cm^2	Potential to achieve 10 mA/cm^2 in 2 electrode assembly

	HER	OER	
Co-3Mo-B	66	320	1.69
Co_2B-500[29]	-	380	1.81
NiMo NAs/Ti[30]	92	310	1.64
NiP/NF[31]	80	309	1.67
$Ni_{0.33}Co_{0.67}S_2$[16]	88	330 (onset)	1.65 (for 5 mA/cm2)
FeP nanotubes[32]	120	288	1.69
Co-Se/Ti[33]	121	292	1.65
Co NPs/N-Carbon[34]	298	370	1.64
CoP/MNA[35]	54	290	1.62
CoP NS/C[36]	111	277	1.54
CoP/NC[37]	191	354	1.55 (onset)
$Fe_{10}Co_{40}Ni_{40}P$[38]	68	250	1.57
Fe_2Ni_2N[39]	180	-	1.65
nanoporous $(Co_{0.52}Fe_{0.48})_2P$[40]	64	270	1.53
Ni_2P/Ni/NF[41]	98	200	1.49

Table S4. Comparison of recent transition-metal based bifunctional electrocatalystsactive in alkaline media.

References:

1. Y. Sun, C. Liu, D. C. Grauer, J. Yano, J. R. Long, P. Yang, C. J. Chang, J. Am. Chem. Soc. 135 (2013) 17699−17702.

2. S. Cobo, J. Heidkamp, P. Jacques, J. Fize, V. Fourmond, L. Guetaz, B. Jousselme, V. Ivanova, H. Dau, S. Palacin, M. Fontecave, V. Artero, Nat. Mater. 11 (2012) 802-807.

3. J. Tian, Q. Liu, A. M. Asiri, X. Sun, J. Am. Chem. Soc. 136 (2014)7587–7590.

4. P. D. Tran, M. Nguyen, S. S. Pramana, A. Bhattacharjee, S. Y. Chiam, J. Fize, M. J. Field, V. Artero, L. H. Wong, J. Loo,J. Barber, Energy Environ. Sci. 5 (2012) 8912-8916.

5. L. Chen, M. Wang, K. Han, P. Zhang, F. Gloaguen, L. Sun, Energy Environ. Sci. 7 (2014) 329–334.

6. Z. Pu, Q. Liu, P. Jiang, A. M. Asiri, A. Y. Obaid,X. Sun, Chem. Mater.,26 (2014) 4326−4329.

7. Z. Pu, C. Tang,Y. Luo, Int. J. Hydrogen Energy40 (2015) 5092-5098.

8. J. F. Callejas, J. M. McEnaney, C. G. Read, J. C. Crompton, A. J. Biacchi, E. J. Popczun, T. R. Gordon, N. S. Lewis, R. E. Schaak, ACS Nano8 (2014) 11101-11107.

9. J. Tian, Q. Liu, Y. Liang, Z. Xing, A. M. Asiri,X. Sun, ACS Appl. Mater. Interfaces 6 (2014) 20579-20584.

10. Y. Liang, Q. Liu, A. M. Asiri, X. Sun,Y. Luo, ACS Catal.,4 (2014) 4065-4069.

11. W. Cui, Q. Liu, Z. Xing, A. M. Asiri, K. A. Alamry,X. Sun, Applied Catalysis B: Environmental 164 (2015) 144–150.

12. H. Du, S. Gu, R. Liu,C. M. Li, J. Power Sources 278 (2015), 540-545.

13. Z. Pu, Q. Liu, A. M. Asiri,X. Sun, ACS Appl. Mater. Interfaces 6 (2014) 21874-21879.

14. Y. Hou, B. Zhang, Z. Wen, S. Cui, X. Guo, Z. He,J. Chen, J. Mater. Chem. A 2 (2014) 13795-13800.

15. C. Tang, Z. Pu, Q. Liu, A. M.Asiri,X. Sun, Electrochim. Acta153 (2015) 508–514.

16. Z. Peng, D. Jia, A. Al-Enizi, M. A. A. Elzatahry, G. Zheng, Adv. Energy Mater. 5 (2015) 1402031.

17. L. L. Feng, G. D. Li, Y. Liu, Y. Wu, H. Chen, Y. Wang, Y. C. Zou, D. Wang,X. Zou, ACS Appl. Mater. Interfaces 7 (2015) 980−988.

18. X. Liu, S. Cui, Z. Sun, P. Du, Chem. Comm. 51 (2015) 12954-12957.

19. Y. Liu, G. Yu, G. D. Li, Y. Sun, T. Asefa, W. Chen, X. Zou, Angew. Chem. Int. Ed. 54 (2015) 1-6.

20. K. Zhang, Y. Zhao, D. Fu, Y. Chen, J. Mater. Chem. A 3 (2015) 5783-5788.

21. H. W. Liang, S. Bruller, R. Dong, J. Zhang, X. Feng, K. Mullen, Nat. Comm. 6 2015.

22. M. Gong, W. Zhou, M. C. Tsai, J. Zhou, M. Guan, M. C. Lin, B. Zhang, Y. Hu, D. Y. Wang, J. Yang, S. J. Pennycook, B. J. Hwang, H. Dai, Nat. Comm., 5 (2014) 1-6.

23. J. R. McKone, B. F. Sadtler, C. A. Werlang, N. S. Lewis,H. B. Gray, ACS Catal. 3 (2013) 166-169.

24. A. B. Laursen, K. R. Patraju, M. J. Whitaker, M. Retuerto, T. Sarkar, N. Yao, K. V.Ramanujachary, M. Greenblatt,G. C. Dismukes, Energy Environ. Sci. 8 (2015) 1027-1034.

25. H. Fei, Y. Yang, Z. Peng, G. Ruan, Q. Zhong, L. Li, E. L. G. Samuel, J. M. Tour, ACS Appl. Mater. Interfaces 7 (2015) 8083-8087.

26. P. Zhang, M. Wang, Y. Yang, T. Yao, H. Han, L. Sun, Nano Energy19 (2016) 98-107.

27. S. Gupta, N. Patel, R. Fernandes, R. Kadrekar, A. Dashora, A. K. Yadav, D. Bhattacharyya, S. N. Jha, A. Miotello, D. C. Kothari, Appl. Cat. B: Environ. 192 (2016) 126-133.

28. D. Merki, H. Vrubel, L. Rovelli, S. Fierro,X. Hu, Chem. Sci. 3 (2012) 2515-2525.

29. J. Masa, P. Weide, D. Peeters, I. Sinev, W. Xia, Z. Sun, C. Somsen, M. Muhler, W. Schuhmann, Adv. Energy Mater. (2016) 1502313.

30. J. Tian, N. Cheng, Q. Liu, X. Sun, Y. He,A. M. Asiri, J. Mater. Chem. A 3 (2015) 20056-20059.

31. C. Tang, A. M. Asiri, Y. Luo, X. Sun, ChemNanoMat1 (2015) 558-561.

32. Y. Yan, B. Y. Xia, X. Ge, Z. Liu, A. Fisher, X. Wang, Chem. Eur. J., 21 (2015) 1-7.

33. T. Liu, Q. Liu, A. M. Asiri, Y. Luo, X. Sun, Chem. Commun.51 (2015) 16683-16686.

34. X. Li, Z. Niu, J. Jiang, L. Ai, J. Mater. Chem. A 4 (2016) 3204-3209.

35. Y. P. Zhu, Y. P. Liu, T. Z. Ren, Z. Y. Yuan, Adv. Funct. Mater. 25 (2015) 7337-7347.

36. J. Chang, L. Liang, C. Li, M. Wang, J. Ge, C. Liu,W. Xing, Green Chem. (2016).

37. B. You, N. Jiangn, M. Sheng, S. Gul, J. Yano,Y. Sun, Chem. Mater. 27 (2015) 7636-7642.

38. Z. Zhang, J. Hao, W. Yang, J. Tang, RSC Adv.6(2016) 9647-9655.

39. M. Jiang, Y. Li, Z. Lu, X. Sun,X. Duan, Inorg. Chem. Front.(2016).

40. Y. Tan, H. Wang, P. Liu, Y. Shen, C. Cheng, A. Hirata, T. Fujita, Z. Tang, M. Chen, Energy Environ. Sci. (2016) DOI:10.1039/C6EE01109H.

41. B. You, N. Jiang, M. Sheng, M. W. Bhushan, Y. Sun,ACS Catal. 6(2) (2015) 714-721.